APPLIED PHYSICS

Atomic–layer–confined multiple quantum wells enabled by monolithic bandgap engineering of transition metal dichalcogenides

Yoon Seok Kim[1]*, Sojung Kang[2]*, Jae-Pil So[3], Jong Chan Kim[4], Kangwon Kim[5], Seunghoon Yang[1], Yeonjoon Jung[6], Yongjun Shin[6], Seongwon Lee[3], Donghun Lee[1], Jin-Woo Park[2], Hyeonsik Cheong[5], Hu Young Jeong[7], Hong-Gyu Park[1,3], Gwan-Hyoung Lee[6,8,9,10]†, Chul-Ho Lee[1,11]†

Quantum wells (QWs), enabling effective exciton confinement and strong light-matter interaction, form an essential building block for quantum optoelectronics. For two-dimensional (2D) semiconductors, however, constructing the QWs is still challenging because suitable materials and fabrication techniques are lacking for bandgap engineering and indirect bandgap transitions occur at the multilayer. Here, we demonstrate an unexplored approach to fabricate atomic–layer–confined multiple QWs (MQWs) via monolithic bandgap engineering of transition metal dichalcogenides and van der Waals stacking. The WO_X/WSe_2 hetero-bilayer formed by monolithic oxidation of the WSe_2 bilayer exhibited the type I band alignment, facilitating as a building block for MQWs. A superlinear enhancement of photoluminescence with increasing the number of QWs was achieved. Furthermore, quantum-confined radiative recombination in MQWs was verified by a large exciton binding energy of 193 meV and a short exciton lifetime of 170 ps. This work paves the way toward monolithic integration of band-engineered heterostructures for 2D quantum optoelectronics.

INTRODUCTION

Two-dimensional (2D) semiconducting transition metal dichalcogenides (TMDs) have attracted enormous attention because of their exceptional optical properties such as direct bandgap transition, large exciton binding energy, and strong light-matter interaction at the ultimate thickness limit (*1*–*5*). Such remarkable features show great potential for applications in high-performance light-emitting devices such as light-emitting diodes (LEDs) (*6*–*8*), lasers (*9*–*11*), and single-photon emitters (*12*–*14*). Nevertheless, high efficiency in the luminescence of those 2D semiconductors is inherently limited to the monolayer regime owing to indirect-to-direct bandgap transitions (*3*, *5*); in addition, intrinsic high quantum yield should be realized for practical applications of those 2D semiconductors (*15*–*18*).

The quantum well (QW) structure is the basic unit used for luminescence enhancement in epitaxial semiconductor heterostructures (*19*). However, the QW structure is difficult to implement with the use of semiconductor TMDs as the light-emitting layer owing to a lack of large-bandgap materials for construction of type I band alignment and the facile fabrication methods compatible with these atomically thin materials (*20*, *21*). In this regard, layered hexagonal boron nitride (*h*-BN) with a wide bandgap has been used as a barrier for fabrication of QWs based on monolayer TMDs through multiple stacking processes (*6*). Although it has merit in forming atomically sharp heterointerfaces without constraints in lattice commensurability, due to the elemental difference between *h*-BN and TMDs, there are limitations in using *h*-BN as a counter material for conventional bandgap engineering based on compositional alloying (*22*). Meanwhile, other large bandgap oxides, such as HfO_2 and Al_2O_3, have difficulties in forming high-quality interfaces with TMDs owing to incompatibilities in both materials and deposition processes (*23*). Considering these issues, a facile fabrication of the TMD-based multiple QWs (MQWs) that enables both confining of excitons and enlarging of active volume remains a considerable challenge.

Here, we report an unexplored strategy of monolithic bandgap engineering of TMDs to fabricate atomic–layer–confined MQWs based on 2D semiconductors. The type I band-aligned WO_X/WSe_2 hetero-bilayer is achieved by layer-by-layer oxidation of WSe_2, which renders a QW building block for fabricating the stacked MQWs. Our approach allows decoupling between adjacent direct bandgap monolayers without indirect band transitions and a superlinear increase of photoluminescence (PL) with increasing the number of 2D QWs in a vertical heterostructure.

RESULTS AND DISCUSSION

Monolithic bandgap engineering of WSe_2 for MQWs

Figure 1A schematically presents the atomic structure of MQWs consisting of WSe_2 monolayer QWs confined by WO_X barrier layers. The corresponding band diagram is depicted in Fig. 1B, which allows for exciton confinement in the atomic WSe_2 layers. The MQWs with different number of QWs, such as single QW (SQW), double QWs (DQWs), and triple QWs (TQWs), were fabricated by repeatedly stacking the WO_X/WSe_2 hetero-bilayers in sequence. (See Materials

[1]KU-KIST Graduate School of Converging Science and Technology, Korea University, Seoul, 02841, Republic of Korea. [2]Department of Materials Science and Engineering, Yonsei University, Seoul 03722, Republic of Korea. [3]Department of Physics, Korea University, Seoul 02841, Republic of Korea. [4]Department of Materials Science and Engineering, Ulsan National Institute of Science and Technology (UNIST), Ulsan 44919, Republic of Korea. [5]Department of Physics, Sogang University, Seoul 04107, Republic of Korea. [6]Department of Materials Science and Engineering, Seoul National University, Seoul 08826, Republic of Korea. [7]UNIST Central Research Facilities (UCRF), Ulsan National Institute of Science and Technology (UNIST), Ulsan 44919, Republic of Korea. [8]Research Institute of Advanced Materials (RIAM), Seoul National University, Seoul 08826, Republic of Korea. [9]Institute of Engineering Research, Seoul National University, Seoul 08826, Republic of Korea. [10]Institute of Applied Physics, Seoul National University, Seoul 08826, Republic of Korea. [11]Department of Integrative Energy Engineering, Korea University, Seoul 02841, Republic of Korea.
*These authors contributed equally to this work.
†Corresponding author. Email: gwanlee@snu.ac.kr (G.-H.L.); chlee80@korea.ac.kr (C.-H.L.)

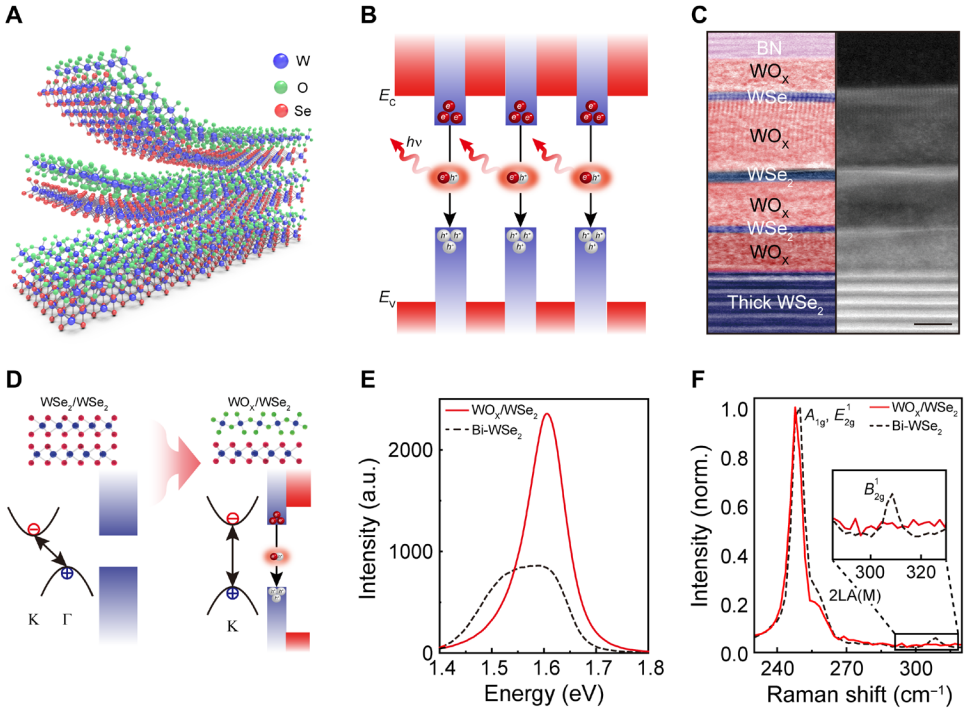

Fig. 1. Atomic–layer–confined MQWs based on monolithic bandgap engineering of WSe_2. (**A**) Schematic illustration of MQWs with stacking of the WO_X/WSe_2 hetero-bilayer as a building block. (**B**) Energy band diagram for MQWs consisting of the WSe_2 QW (blue) and the WO_X quantum barrier (red). This type I structure leads to effective carrier confinement in the QW. E_C and E_V indicate the conduction band edge and valence band edge, respectively. (**C**) Cross-sectional bright-field (left) and corresponding high-angle annular dark-field (right) STEM (scanning transmission electron microscopy) images of the triple QWs (TQWs). Scale bar, 2 nm. (**D**) Schematic illustration of monolithic band engineering of the bilayer WSe_2, showing the transition of a band structure and energy band alignment via oxidation. (**E**) PL spectra and (**F**) Raman spectra of the layer-by-layer oxidized WO_X/WSe_2 hetero-bilayer and the pristine WSe_2 bilayer. The inset in (F) shows the magnified B^1_{2g} mode in Raman spectra. a.u., arbitrary units.

and Methods and the Supplementary Materials for the detailed fabrication process.) Figure 1C shows cross-sectional bright-field and high-angle annular dark-field scanning transmission electron microscopy (STEM) images of the representative TQWs experimentally demonstrated in this work.

The basic building block of WO_X/WSe_2 is monolithically fabricated through layer-by-layer oxidation of the bilayer WSe_2 using ultraviolet (UV)–ozone treatment at 100°C for 60 min (*24*, *25*). Through this facile and low-temperature process, the topmost layer undergoes the structural phase transition from crystalline WSe_2 to amorphous WO_X with a slight increase of thickness. As verified by STEM and atomic force microscopy (AFM) (fig. S1A), the WO_X oxidized from monolayer WSe_2 showed a uniform thickness of 1.5 to 2 nm despite slight variation resulted from the process-induced deformation or nonstoichiometric/inhomogeneous oxidation (*26*). Even after oxidation, WO_X maintains an atomically flat surface with a roughness of 60 pm, comparable to the smoothness of WSe_2 (fig. S1B). It is noteworthy that such a smooth surface and uniform thickness of WO_X enables the fabrication of MQWs with clean hetero-interfaces and uniform tunnel barriers via multiple stacking of building blocks.

The monolithic oxidation not only induces phase conversion of the top WSe_2 layer into the large bandgap WO_X layer but also leads to indirect-to-direct bandgap transition in the bottom WSe_2 layer (Fig. 1D). As compared in Fig. 1E, the as-exfoliated bilayer WSe_2 and the oxidized WO_X/WSe_2 hetero-bilayer showed distinctive steady-state PL spectra. The bilayer WSe_2 exhibits two main PL peaks at 1.55 and 1.60 eV, which are associated with indirect transition and A-exciton emission, respectively (*27*). Meanwhile, upon oxidation of the topmost WSe_2 layer, the A-exciton emission substantially increased with the quenched indirect transition. This implies that the bottom WSe_2 monolayer of the oxidized hetero-bilayer has the direct bandgap characteristic, as observed in the as-exfoliated monolayer. However, the dominant PL peak exhibited a red shift by ~50 meV relative to the neutral exciton peak of the pristine WSe_2 monolayer, which is probably due to the oxidation-induced hole doping (*24*). This peak shift disappeared along with further enhanced PL intensity after the wet transfer process assisted by hydrofluoric acid (HF) (fig. S2), which is similar to the previous reports that defect passivation by HF results in de-doping (*17*, *28*). To further verify such an effect, the Urbach energy (E_0), indicative of the degree of band tailing induced by structural disorders and impurities, was evaluated (fig. S3) (*15*). The extracted value decreased from 25.0 to 17.6 meV after the HF-mediated transfer, indicating the reduced disorder from potential fluctuation and the improved band-edge sharpness (*29*). Note that there was a slight reduction in the absolute PL intensity after processing presumably due to its variation resulting from different doping states (*24*). However, the degree of reduction was not so substantial that the internal quantum efficiency (IQE) was maintained in the SQW as discussed below in the temperature-dependent PL characteristics.

The monolayer characteristics of the oxidized WO_X/WSe_2 hetero-bilayer was also investigated by Raman spectroscopy (Fig. 1F). The as-exfoliated bilayer showed two characteristic peaks at 250 cm^{-1}

(A_{1g} and E^1_{2g}) and 310 cm^{-1} (B^1_{2g}). After oxidation, the B^1_{2g} peak, a fingerprint mode of the bilayer originated from interlayer coupling, diminished, maintaining the A_{1g} and E^1_{2g} modes. This also implies that the WO_X/WSe_2 hetero-bilayer behaves like a monolayer because the B^1_{2g} mode is inactive at the monolayer limit (*24*). The abovementioned changes in the structural and optical properties induced by monolithic oxidation have been consistently observed for both mechanically exfoliated bilayer and chemical vapor–deposited bilayer samples (figs. S4 and S5).

Band alignment of the WO_X/WSe_2 hetero-bilayer

To further confirm the energy band modulation in the WO_X/WSe_2 hetero-bilayer and its potential as a building block for forming the QW, we investigated the band alignment between WO_X and WSe_2 by using PL, UV-visible (UV-Vis) absorption, and UV photoelectron spectroscopy (UPS). For those spectroscopic studies, the large-scale homogeneous monolayer WSe_2 films grown by metal-organic chemical vapor deposition (MOCVD) were used. As shown in the PL and UV-Vis absorption spectra (Fig. 2A), the optical bandgap of WSe_2 is determined to be 1.65 eV, which is in agreement with previous studies. Meanwhile, as extracted by the Tauc plot in Fig. 2B, the bandgap of the WO_X oxidized from monolayer WSe_2 was 3.28 eV, which is comparable to that of bulk WO_X (*30*). The measured work functions ($E_{VAC} - E_F$) of WSe_2 and WO_X were 4.65 and 5.15 eV, respectively, which were obtained by taking the difference between photon energy (21.2 eV for He I) and photoemission onset (16.55 and 16.05 eV for each layer) from the secondary electron cutoffs in the UPS spectra (Fig. 2C). The energy differences between the valence band edge and Fermi level ($E_F - E_V$) were 1.35 eV for WSe_2 and 2 eV for WO_X, which were estimated from the binding energy onsets in Fig. 2D. By combining all the results, as depicted in Fig. 2E, the constructed band structure between the WO_X and monolayer WSe_2 shows type I alignment before and after aligning the Fermi level, suggesting that both electrons and holes can be effectively confined in a WSe_2 monolayer. This formation of type I band alignment, combined with the indirect-to-direct bandgap transition, allows us to define the layer-by-layer oxidation process as monolithic bandgap engineering, enabling the use of the WO_X/WSe_2 hetero-bilayer as a building block for MQW structures.

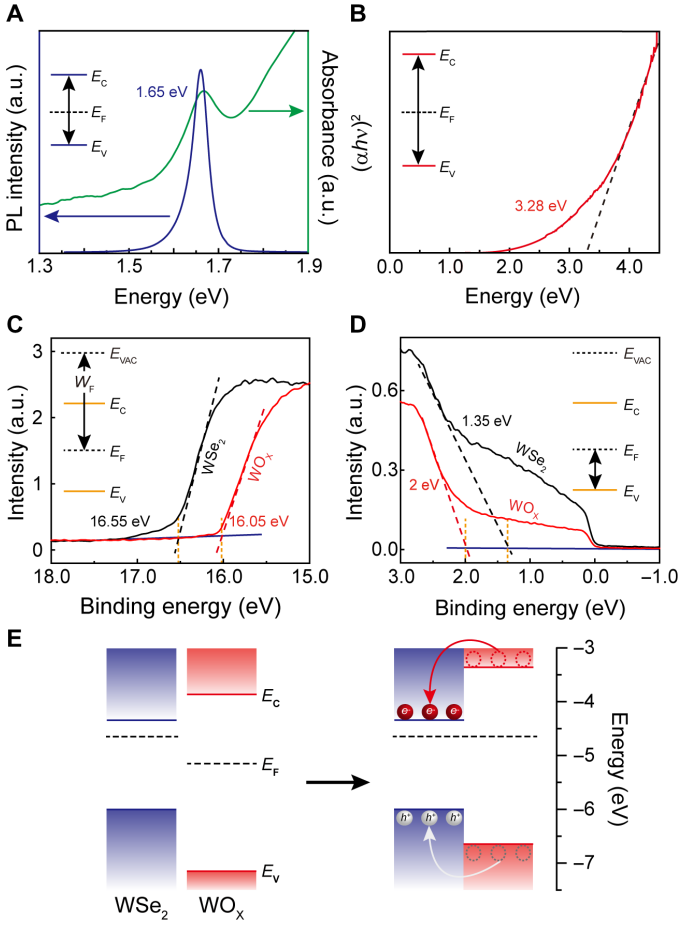

Fig. 2. Analysis of the QW band structure of WO_X/WSe_2. (**A**) PL (blue solid line) and UV-Vis absorption (green solid line) spectra of the pristine WSe_2 monolayer, exhibiting the optical bandgap at 1.65 eV. (**B**) Tauc plot for the WO_X directly oxidized from the WSe_2 monolayer. The estimated bandgap is 3.28 eV. (**C**) UPS spectra of the secondary electron edge for the pristine WSe_2 (black solid line) and the oxidized WO_X (red solid line); the extracted work functions are 4.65 and 5.15 eV, respectively. (**D**) UPS spectra at the low binding energy region near E_F for the pristine WSe_2 (black solid line) and the oxidized WO_X (red solid line). The energy difference of $E_F - E_V$ is estimated from the onset of the low binding energy, which are 1.35 and 2 eV for WSe_2 and WO_X, respectively. (**E**) Constructed band diagrams with type I band alignment between WO_X and WSe_2 before (left) and after (right) aligning the E_F.

Fabrication and optical characterization of MQWs

The MQWs were fabricated by sequentially stacking the building blocks of WO_X/WSe_2 hetero-bilayers as shown in Fig. 3A. For the MQWs with different numbers of stacked QWs, the optical and structural characteristics were investigated by PL and low-frequency Raman spectroscopy. The steady-state PL spectra of Fig. 3B show that the PL intensity of the MQWs increases with the stacking number of QWs. A slight red shift of ~20 meV was observed in DQWs and TQWs, which might be due to the transfer process–induced tensile strain (*31*). Nevertheless, unlike the conventional MQWs, the PL peak was barely unchanged because the optical bandgap is strongly affected by large exciton binding energy in the ultimately quantum-confined 2D structure, which was similarly observed in *h*-BN/TMD QW structures (*6*). This consistent bandgap might be also attributed to bandgap renormalization of WSe_2 as previously reported (*32*, *33*).

Each MQW region showed uniform emission and incremental PL intensity with stacking of the QWs, as visualized in the spatially resolved PL mapping image (Fig. 3A). To verify the effectiveness of WO_X as a barrier, we compared the PL behaviors of MQWs with those of the artificially stacked multilayers, including bilayer (1L WSe_2/1L WSe_2) and trilayer (1L WSe_2/1L WSe_2/1L WSe_2). The multilayers differently exhibited the decrease of PL with stacking of the monolayers and emergence of the B^1_{2g} Raman mode, which indicates that the monolayers in the stack have a strong interlayer coupling (fig. S6). In contrast, interaction between the separated monolayers by the oxidized WO_X layer in MQWs is effectively suppressed so that the WSe_2 monolayers act as a light-emitting QW confined by the large bandgap WO_X barrier with type I band alignment.

The PL enhancement of MQWs was consistently observed for both mechanically exfoliated and chemical vapor–deposited WSe_2 bilayer samples (fig. S7 for mechanically exfoliated MQWs). Statistically, when compared to the SQW, DQWs and TQWs exhibited approximately twofold and fivefold increase in the integrated

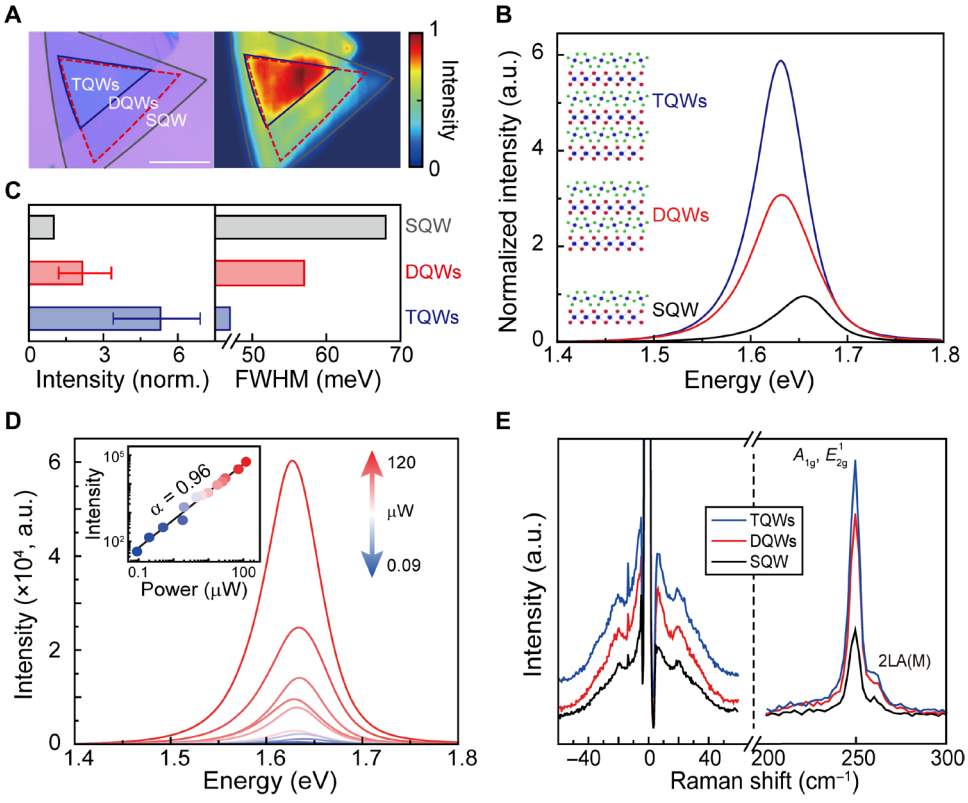

Fig. 3. Optical characteristics of MQWs. (**A**) Optical image (left) and spatially resolved PL map (right) of the step-like stacked MQWs. The SQW, DQWs, and TQWs areas are indicated by gray, red, and blue triangles, respectively. Scale bar, 10 μm. (**B**) PL spectra for the SQW (black line), DQWs (red line), and TQWs (blue line). (**C**) Histograms for the integrated PL intensity (left) and full width half maximum (FWHM) (right) for the SQW (gray), DQWs (red), and TQWs (blue). The integrated intensity is normalized to that of the SQW, and the values are 2.16 ± 0.96 (DQWs) and 5.31 ± 1.90 (TQWs). (**D**) Power-dependent PL spectra of the TQWs at 300 K. The excitation power varies from 0.09 to 120 μW. The inset shows the log scale plot of the integrated intensity as a function of power, fitted by the power law with the exponent of α = 0.96. (**E**) Low-frequency (left) and high-frequency (right) Raman spectra of SQW, DQWs, and TQWs.

PL intensity, respectively (Fig. 3C, left). Such a superlinear enhancement of PL is attributed to not only the confinement of WSe_2 monolayers but also the effective radiative recombination in MQWs. To further reveal other origins, we performed the numerical simulation on light extraction efficiency from MQWs, which is based on the Fresnel equation considering the transmission, reflection, and absorption for the emitted light traveling across the different mediums and their interfaces (*34*). According to the results, the extracted luminescence of SQW, DQWs, and TQWs increases in a superlinear manner because of multiple reflections at the interfaces of the periodic MQW structures (fig. S8). As another possible explanation, the WSe_2 QW layer further away from the SiO_2/Si substrate can contribute more to the PL because the substrate has substantial potential fluctuation by trap sites and charge impurities (*35*).

In addition, the full width at half maximum (FWHM) of the PL decreased from 68 meV (SQW) to 47 meV (TQWs) as the number of QWs increased (Fig. 3C, right). The absence of spectral broadening supports that no notable generation of structural defects occurred during the oxidation and multiple stacking processes, as already verified in the cross-sectional STEM image of Fig. 1C (*36*). Furthermore, in the power-dependent PL spectra (Fig. 3D), the integrated PL intensity increased as the excitation power varied from 0.09 to 120 μW, following the power law of $I_{int.} \propto P^{\alpha}$, where $I_{int.}$, P, and α are the integrated PL intensity, incident laser power, and exponent factor, respectively. α is extracted to be 0.96 for TQWs (see also fig. S9 for the SQW), which is larger than that of a pristine WSe_2 monolayer. Particularly, the exponent factor close to unity suggests that the band-to-band transition is dominant with the suppressed surface recombination in MQWs (*37*).

The preservation of the monolayer characteristics in MQWs is further unveiled by Raman spectroscopy. Particularly, in the low-frequency Raman spectra (Fig. 3E, left), the distinctive peak at 20 cm^{-1} is due to the laser-induced resonance effect that is most prominent in the monolayer. No interlayer vibration mode is observed for any of the three QWs, indicating the decoupling behavior between adjacent monolayers (*38*). Moreover, in the high-frequency Raman spectra (Fig. 3E, right), there is no shift of the monolayer characteristic peaks, including the E^1_{2g} and A_{1g} modes around 250 cm^{-1} and the 2LA(M) mode at 260 cm^{-1}, as well as no emergence of additional peaks. This also suggests that each WSe_2 layer in MQWs is sufficiently decoupled, maintaining its monolayer characteristics, and noticeable doping and strain have not been induced during multiple stacking.

Exciton dynamics in MQWs

To gain in-depth understanding on the radiative recombination in MQWs, we performed temperature-dependent and time-resolved PL measurements. Figure 4A shows the PL spectra of the SQW at various temperatures from 4 to 300 K. As the temperature decreased, the neutral exciton peak (X^0) was sustained even at low

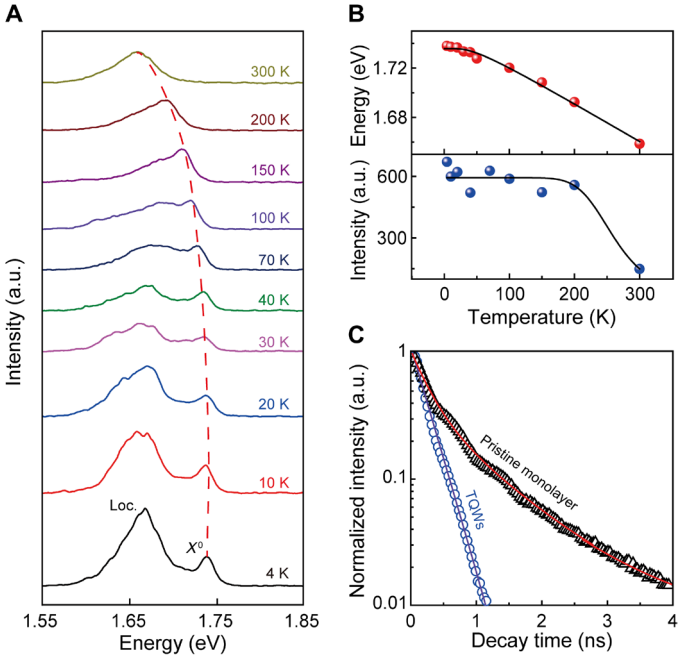

Fig. 4. Exciton dynamics in MQWs. (**A**) Temperature-dependent PL spectra from 4 to 300 K. The red dashed line indicates the shift of the neutral exciton peak. The defect-mediated localized peak and the neutral exciton peak are denoted by Loc. and X^0, respectively. (**B**) Plots of the X^0 energy (top) and the integrated intensity (bottom) as a function of temperature. Solid black lines are fitted with the modified Varshni equation (top) and the Arrhenius equation (bottom). (**C**) Time-resolved PL spectra of the pristine WSe_2 monolayer (black triangles) and TQWs (blue open circles) at 300 K. The curves are fitted with the biexponential decay (red solid line) for WSe_2 and single-exponential decay function (purple solid line) for TQWs.

temperatures, although it exhibited a blue shift from 1.65 eV at 300 K to 1.73 eV at 4 K (*39*, *40*). Meanwhile, a broad PL peak of ~1.66 eV, related to the localized defect states, emerged below ~100 K and increased with decreasing temperature. This localized PL peak was similarly observed in the as-exfoliated monolayer WSe_2 in previous studies, owing to naturally existing and process-induced defects (*37*, *39*). In addition, we investigated the IQE, estimated from the ratio of integrated PL intensities between low temperature (4 K) and room temperature (fig. S10) (*41*). The extracted IQE value of the pristine monolayer and SQW was 39.7 and 40.1%, respectively. These results suggest that the SQW has optical quality comparable to that of the as-exfoliated monolayer, although oxidation may induce some defects.

The variation of the X^0 peak position extracted by Gaussian fitting was well fitted by the modified Varshni equation that describes the temperature dependence of a semiconductor bandgap (Fig. 4B, top) (*42*, *43*)

$$E_g(T) = E_g(0) - S\langle\hbar\omega\rangle\left[\coth\left(\frac{\langle\hbar\omega\rangle}{2k_BT}\right) - 1\right]$$

where $E_g(0)$, S, and $\langle\hbar\omega\rangle$ are the bandgap at $T = 0$ K, dimensionless constant for the strength of the electron-phonon coupling, and average acoustic phonon energy in electron-phonon interactions, respectively. The acoustic phonon energy for SQW obtained by fitting, $\langle\hbar\omega\rangle$ = 10.5 meV, is smaller than that of the WSe_2 monolayer (14.5 meV). From the plot of the intensity of X^0 as a function of temperature (Fig. 4B, bottom), the exciton binding energy (E_b) was estimated by using the one-channel Arrhenius equation of $I(T) = I_0/(1 + A \exp(E_b/k_BT))$, where I_0, k_B, and A are the PL intensity at $T = 0$ K, the Boltzmann constant, and the fitting parameter, respectively. The extracted E_b for SQW was 193 meV. This is lower than that of the as-exfoliated monolayer WSe_2 in air (370 meV) because E_b is inversely proportional to the square of the dielectric constant of the surrounding material, as described in $E_{b,exc}^{(n)} = \mu e^4/\left(2\hbar\varepsilon_{eff}^2(n-1/2)^2\right)$, where μ and ε_{eff} are the effective mass of the carriers and the effective dielectric constant, respectively (*44*, *45*). However, its value is much larger than those of III-V semiconductor QWs and presumably larger than expected considering that the dielectric constant of WO_X is approximately 3 to 5 (*46*, *47*). Such large E_b, in addition to low $\langle\hbar\omega\rangle$, can be attributed to effective exciton confinement in the monolithically fabricated QW structure.

Furthermore, we examined the recombination dynamics of excitons in MQWs. Figure 4C shows the time-resolved PL spectra of the as-exfoliated monolayer WSe_2 and the stacked TQWs. The monolayer WSe_2 was fitted by a biexponential decay curve. The extracted lifetimes for slow and fast decay processes were $\tau_{mono,slow}$ = 669 ps and $\tau_{mono,fast}$ = 179 ps, which are responsible for the radiative and nonradiative recombination, respectively. In the case of TQWs, however, we observed a single-exponential decay with a short radiative lifetime of τ_{TQWs} = 170 ps. As further verified by comparing the low-temperature PL spectra, the short-lived emission observed in MQWs may not be dominated by the localized defects (fig. S11), which is rather attributed to the effective confinement of excitons in the WSe_2 QW layers and the suppression of surface recombination by the WO_X dielectric encapsulation. (*48*, *49*). It should be noted that although our experimental results revealed the effective exciton confinement in the type I band-aligned QWs, the detailed subband structures in MQWs and interaction among QWs have not been thoroughly investigated. To clarify that, an in-depth theoretical calculation and advanced band-structure measurements of our MQWs will be required as a further investigation (*50*).

In summary, we successfully demonstrated the monolithic fabrication of atomic–layer–confined MQWs and the exciton confinement effect in their luminescence characteristics. The bandgap-modulated WO_X/WSe_2 hetero-bilayer, which was monolithically oxidized from the WSe_2 bilayer, exhibited the type I band alignment, providing a building block for fabricating the stacked MQWs. Unlike the stacking of monolayer TMDs, in the stacked MQWs, we observed the superlinear increase in PL intensity as the number of QWs increased; this could be attributed to the decoupling between adjacent WSe_2 monolayers by the WO_X barrier layer, as confirmed by the PL and Raman characterization. Furthermore, owing to the effective confinement of excitons in 2D MQWs, the relatively large exciton binding energy of 193 meV and the fast exciton lifetime of 170 ps were revealed by temperature-dependent and time-resolved PL studies. Our work suggests a facile and unexplored approach to engineer the bandgap and energy band alignment of TMDs, thus presenting a breakthrough to implement monolithic 2D heterostructures for high-efficiency quantum optoelectronics.

MATERIALS AND METHODS

Sample preparation

Monolayer and bilayer WSe_2 samples were prepared through two different methods: CVD growth (including MOCVD) and mechanical exfoliation from bulk crystal (HQ Graphene). The number of

layers was determined by optical characterization and AFM (figs. S12 and S13). For the fabrication of the MQWs, three sets of WO_X/WSe_2 were separately fabricated onto 285-nm-thick SiO_2/Si substrates by oxidizing the bilayer WSe_2 in a UV-ozone chamber (UV-1, Samco Inc.) under the process conditions at 100°C for 60 min without UV illumination. After the oxidation process, each WO_X/WSe_2 hetero-bilayer was sequentially stacked into the MQWs using the HF-mediated vdW transfer method (fig. S2). The stacked MQW samples were annealed in ultrahigh vacuum (~3×10^{-7} torr) at 450°C for 12 hours to remove polymer residues and nanobubbles.

Sample characterization

AFM (Park systems, NX-10) was used to characterize the surface morphology and the thickness of the samples. For the high-resolution cross-sectional STEM samples, the *h*-BN/TQWs/WO_X/WSe_2 (few-layer) heterostructure was milled with a focused ion beam (FEI Helios NanoLab 450). Then, cross-sectional HR-STEM images were obtained using a FEI Titan G2 60-300 with a 200-kV operating voltage.

Optical characterization

The absorption spectra were measured with a UV-Vis spectrophotometer (8453E, Agilent). The UPS measurements were conducted using a PHI 500 VersaProbe (ULVAC-PHI) with a monochromatic Al Kα x-ray source (1486.6 eV). High-frequency Raman and steady-state PL measurements were performed using an optical microscope equipped with a 532-nm continuous-wave laser (excitation power of 120 μW) and a monochromator (Andor, Solis 303i). The signal was collected by an objective lens (100×, N.A. = 0.9) and dispersed by 1200 and 300 line mm^{-1} grating for high-frequency Raman and steady-state PL measurements, respectively. For the spatially resolved PL mapping, the sample was scanned in the *X*-*Y* plane by a 1 μm per step resolution using the motorized stage. Low-frequency Raman measurements were performed using a custom-built confocal microscope system with volume holographic filters (Optigrate) with a 514.5-nm continuous-wave laser (excitation power of 100 μW) as the excitation source. The signal was dispersed with a Jobin-Yvon Horiba iHR550 spectrometer with 2400 line mm^{-1} grating. Temperature-dependent PL (from 4 K to 300 K) was carried out in a He-flow cryostat (Montana Instruments s50) with a 532-nm continuous-wave laser (excitation power of 40 μW) and a monochromator (Princeton Instruments PIXIS 400 BRX). For time-resolved PL measurements, the emitted photons from the samples were detected by two identical avalanche photodiodes and time tagging electronics (PicoQuant Picoharp 300).

SUPPLEMENTARY MATERIALS

Supplementary material for this article is available at http://advances.sciencemag.org/cgi/content/full/7/13/eabd7921/DC1

REFERENCES AND NOTES

1. K. S. Novoselov, A. Mishchenko, A. Carvalho, A. H. Castro Neto, 2D materials and van der Waals heterostructures. *Science* **353**, aac9439 (2016).
2. L. Britnell, R. M. Ribeiro, A. Eckmann, R. Jalil, B. D. Belle, A. Mishchenko, Y. Kim, R. V. Gorbachev, T. Georgiou, S. V. Morozov, A. N. Grigorenko, A. K. Geim, C. Casiraghi, A. H. C. Neto, K. S. Novoselov, Strong light-matter interactions thin films. *Science* **340**, 1311–1314 (2013).
3. F. Xia, H. Wang, D. Xiao, M. Dubey, A. Ramasubramaniam, Two-dimensional material nanophotonics. *Nat. Photonics* **8**, 899–907 (2014).
4. X. Liu, T. Galfsky, Z. Sun, F. Xia, E. Lin, Y.-H. Lee, S. Kéna-Cohen, V. M. Menon, Strong light–matter coupling in two-dimensional atomic crystals. *Nat. Photonics* **9**, 30–34 (2014).
5. K. F. Mak, C. Lee, J. Hone, J. Shan, T. F. Heinz, Atomically thin MoS_2: A new direct-gap semiconductor. *Phys. Rev. Lett.* **105**, 136805 (2010).
6. F. Withers, O. Del Pozo-Zamudio, A. Mishchenko, A. P. Rooney, A. Gholinia, K. Watanabe, T. Taniguchi, S. J. Haigh, A. K. Geim, A. I. Tartakovskii, K. S. Novoselov, Light-emitting diodes by band-structure engineering in van der Waals heterostructures. *Nat. Mater.* **14**, 301–306 (2015).
7. F. Withers, O. Del Pozo-Zamudio, S. Schwarz, S. Dufferwiel, P. M. Walker, T. Godde, A. P. Rooney, A. Gholinia, C. R. Woods, P. Blake, S. J. Haigh, K. Watanabe, T. Taniguchi, I. L. Aleiner, A. K. Geim, V. I. Fal'Ko, A. I. Tartakovskii, K. S. Novoselov, WSe_2 light-emitting tunneling transistors with enhanced brightness at room temperature. *Nano Lett.* **15**, 8223–8228 (2015).
8. D. H. Lien, M. Amani, S. B. Desai, G. H. Ahn, K. Han, J.-H. He, J. W. Ager III, M. C. Wu, A. Javey, Large-area and bright pulsed electroluminescence in monolayer semiconductors. *Nat. Commun.* **9**, 1229 (2018).
9. Y. Ye, Z. J. Wong, X. Lu, X. Ni, H. Zhu, X. Chen, Y. Wang, X. Zhang, Monolayer excitonic laser. *Nat. Photonics* **9**, 733–737 (2015).
10. S. Wu, S. Buckley, J. R. Schaibley, L. Feng, J. Yan, D. G. Mandrus, F. Hatami, W. Yao, J. Vučković, A. Majumdar, X. Xu, Monolayer semiconductor nanocavity lasers with ultralow thresholds. *Nature* **520**, 69–72 (2015).
11. Y. Liu, H. Fang, A. Rasmita, Y. Zhou, J. Li, T. Yu, Q. Xiong, N. Zheludev, J. Liu, W. Gao, Room temperature nanocavity laser with interlayer excitons in 2D heterostructures. *Sci. Adv.* **5**, eaav4506 (2019).
12. Y.-M. He, G. Clark, J. R. Schaibley, Y. He, M.-C. Chen, Y.-J. Wei, X. Ding, Q. Zhang, W. Yao, X. Xu, C.-Y. Lu, J.-W. Pan, Single quantum emitters in monolayer semiconductors. *Nat. Nanotechnol.* **10**, 497–502 (2015).
13. M. Koperski, K. Nogajewski, A. Arora, J. Marcus, P. Kossacki, M. Potemski, Single photon emitters in exfoliated WSe_2 structures. *Nat. Nanotechnol.* **10**, 503–506 (2014).
14. A. Branny, S. Kumar, R. Proux, B. D. Gerardot, Deterministic strain-induced arrays of quantum emitters in a two-dimensional semiconductor. *Nat. Commun.* **8**, 15053 (2016).
15. M. Amani, D.-H. Lien, D. Kiriya, J. Xiao, A. Azcatl, J. Noh, S. R. Madhvapathy, R. Addou, S. KC, M. Dubey, K. Cho, R. M. Wallace, S.-C. Lee, J.-H. He, J. W. Ager III, X. Zhang, E. Yablonovitch, A. Javey, Near-unity photoluminescence quantum yield in MoS_2. *Science* **350**, 1065 (2015).
16. S. Kang, D. Lee, J. Kim, A. Capasso, H. S. Kang, J.-W. Park, C.-H. Lee, G.-H. Lee, 2D semiconducting materials for electronic and optoelectronic applications: Potential and challenge. *2D Mater.* **7**, 022003 (2020).
17. J. H. Park, A. Sanne, Y. Guo, M. Amani, K. Zhang, H. C. P. Movva, J. A. Robinson, A. Javey, J. Robertson, S. K. Banerjee, A. C. Kummel, Defect passivation of transition metal dichalcogenides via a charge transfer van der Waals interface. *Sci. Adv.* **3**, e1701661 (2017).
18. D.-H. Lien, S. Z. Uddin, M. Yeh, M. Amani, H. Kim, J. W. Ager III, E. Yablonovitch, A. Javey, Electrical suppression of all nonradiative recombination pathways in monolayer semiconductors. *Science* **364**, 468–471 (2019).
19. E. E. Mendez, K. von Klitzing, *Physics and Applications of Quantum Wells and Superlattices* (Springer, 1987).
20. N. R. Wilson, P. V. Nguyen, K. Seyler, P. Rivera, A. J. Marsden, Z. P. L. Laker, G. C. Constantinescu, V. Kandyba, A. Barinov, N. D. M. Hine, X. Xu, D. H. Cobden, Determination of band offsets, hybridization, and exciton binding in 2D semiconductor heterostructures. *Sci. Adv.* **3**, e1601832 (2017).
21. J. Wang, I. Verzhbitskiy, G. Eda, Electroluminescent devices based on 2D semiconducting transition metal dichalcogenides. *Adv. Mater.* **30**, 1802687 (2018).
22. C.-Z. Ning, L. Dou, P. Yang, Bandgap engineering in semiconductor alloy nanomaterials with widely tunable compositions. *Nat. Rev. Mater.* **2**, 17070 (2017).
23. Y. Liu, J. Guo, E. Zhu, L. Liao, S. J. Lee, M. Ding, I. Shakir, V. Gambin, Y. Huang, X. Duan, Approaching the Schottky-Mott limit in van der Waals metal-semiconductor junctions. *Nature* **557**, 696–700 (2018).
24. M. Yamamoto, S. Dutta, S. Aikawa, S. Nakaharai, K. Wakabayashi, M. S. Fuhrer, K. Ueno, K. Tsukagoshi, Self-limiting layer-by-layer oxidation of atomically thin WSe_2. *Nano Lett.* **15**, 2067–2073 (2015).
25. S. Yang, J. Cha, J. C. Kim, D. Lee, W. Huh, Y. Kim, S. W. Lee, H. G. Park, H. Y. Jeong, S. Hong, G.-H. Lee, C.-H. Lee, Monolithic interface contact engineering to boost optoelectronic performances of 2D semiconductor photovoltaic heterojunctions. *Nano Lett.* **20**, 2443–2451 (2020).
26. I. Yadav, S. Jain, S. S. Lamba, M. Tomar, S. Gupta, V. Gupta, K. K. Jain, S. Dutta, R. Chatterjee, Effect of growth and electrical properties of TiO_x films on microbolometer design. *J. Mater. Sci. Mater. Electron.* **31**, 6671–6678 (2020).
27. G. Wang, X. Marie, L. Bouet, M. Vidal, A. Balocchi, T. Amand, D. Lagarde, B. Urbaszek, Exciton dynamics in WSe_2 bilayers. *Appl. Phys. Lett.* **105**, 182105 (2014).
28. H.-V. Han, A.-Y. Lu, L.-S. Lu, J.-K. Huang, H. Li, C.-L. Hsu, Y.-C. Lin, M.-H. Chiu, K. Suenaga, C.-W. Chu, H.-C. Kuo, W.-H. Chang, L.-J. Li, Y. Shi, Photoluminescence enhancement

and structure repairing of monolayer $MoSe_2$ by hydrohalic acid treatment. *ACS Nano* **10**, 1454–1461 (2016).
29. A. Iribarren, R. Castro-Rodríguez, V. Sosa, J. Peña, Band-tail parameter modeling in semiconductor materials. *Phys. Rev. B* **58**, 1907–1911 (1998).
30. H. Zheng, J. Z. Ou, M. S. Strano, R. B. Kaner, A. Mitchell, K. Kalantar-Zadeh, Nanostructured tungsten oxide—Properties, synthesis, and applications. *Adv. Funct. Mater.* **11**, 2175–2196 (2011).
31. O. B. Aslan, M. Deng, T. F. Heinz, Strain tuning of excitons in monolayer WSe_2. *Phys. Rev. B.* **98**, 115308 (2018).
32. M. M. Ugeda, A. J. Bradley, S.-F. Shi, F. H. da Jornada, Y. Zhang, D. Y. Qiu, W. Ruan, S.-K. Mo, Z. Hussain, Z.-X. Shen, F. Wang, S. G. Louie, M. F. Crommie, Giant bandgap renormalization and excitonic effects in a monolayer transition metal dichalcogenide semiconductor. *Nat. Mater.* **13**, 1091 (2014).
33. Z. Qiu, M. Trushin, H. Fang, I. Verzhbitskiy, S. Gao, E. Laksono, M. Yang, P. Lyu, J. Li, J. Su, M. Telychko, K. Watanabe, T. Taniguchi, J. Wu, A. H. C. Neto, L. Yang, G. Eda, S. Adam, J. Lu, Giant gate-tunable bandgap renormalization and excitonic effects in a 2D semiconductor. *Sci. Adv.* **5**, eaaw2347 (2019).
34. E. Hecht, *Optics* (Pearson Education, 2016).
35. W. Xu, D. Kozawa, Y. Zhou, Y. Wang, Y. Sheng, T. Jiang, M. S. Strano, J. H. Warner, Controlling photoluminescence enhancement and energy transfer in WS_2:hBN:WS_2 vertical stacks by precise interlayer distances. *Small* **16**, 1905985 (2020).
36. A. Raja, M. Selig, T. F. Heinz, A. Knorr, C. Schüller, A. Chernikov, T. Korn, G. Berghäuser, P. Nagler, E. Malic, Excitonic linewidth and coherence lifetime in monolayer transition metal dichalcogenides. *Nat. Commun.* **7**, 13279 (2016).
37. Z. Ye, L. Waldecker, E. Y. Ma, D. Rhodes, A. Antony, B. Kim, X.-X. Zhang, M. Deng, Y. Jiang, Z. Lu, D. Smirnov, K. Watanabe, T. Taniguchi, J. Hone, T. F. Heinz, Efficient generation of neutral and charged biexcitons in encapsulated WSe_2 monolayers. *Nat. Commun.* **9**, 3718 (2018).
38. S. Kim, K. Kim, J.-U. Lee, H. Cheong, Excitonic resonance effects and Davydov splitting in circularly polarized Raman spectra of few-layer WSe_2. *2D Mater.* **4**, 045002 (2017).
39. T. Godde, D. Schmidt, J. Schmutzler, M. Aßmann, J. Debus, F. Withers, E. M. Alexeev, O. Del Pozo-Zamudio, O. V. Skrypka, K. S. Novoselov, M. Bayer, A. I. Tartakovskii, Exciton and trion dynamics in atomically thin $MoSe_2$ and WSe_2: Effect of localization. *Phys. Rev. B* **94**, 165301 (2016).
40. T. Yan, X. Qiao, X. Liu, P. Tan, X. Zhang, Photoluminescence properties and exciton dynamics in monolayer WSe_2. *Appl. Phys. Lett.* **105**, 101901 (2014).
41. T.-Y. Seong, J. Han, H. Amano, H. Morkoç, *III-Nitride Based Light Emitting Diodes and Applications* (Springer, 2013).
42. K. J. Lee, B. Turedi, L. Sinatra, A. A. Zhumekenov, P. Maity, I. Dursun, R. Naphade, N. Merdad, A. Alsalloum, S. Oh, N. Wehbe, M. N. Hedhili, C. H. Kang, R. C. Subedi, N. Cho, J. S. Kim, B. S. Ooi, O. F. Mohammed, O. M. Bakr, Perovskite-based artificial multiple quantum wells. *Nano Lett.* **19**, 3535–3542 (2019).
43. J. Huang, T. B. Hoang, M. H. Mikkelsen, Probing the origin of excitonic states in monolayer WSe_2. *Sci. Rep.* **6**, 22414 (2016).
44. A. Chernikov, T. C. Berkelbach, H. M. Hill, A. Rigosi, Y. Li, O. B. Aslan, D. R. Reichman, M. S. Hybertsen, T. F. Heinz, Exciton binding energy and nonhydrogenic Rydberg series in monolayer WS_2. *Phys. Rev. Lett.* **113**, 076802 (2014).
45. K. He, N. Kumar, L. Zhao, Z. Wang, K. F. Mak, H. Zhao, J. Shan, Tightly bound excitons in monolayer WSe_2. *Phys. Rev. Lett.* **113**, 026803 (2014).
46. X. Leng, J. Pereiro, J. Strle, G. Dubuis, A. T. Bollinger, A. Gozar, J. Wu, N. Litombe, C. Panagopoulos, D. Pavuna, I. Božović, Insulator to metal transition in WO_3 induced by electrolyte gating. *NPJ Quantum Mater.* **2**, 35 (2017).
47. R. B. Goldner, K. Wong, G. Foley, P. Norton, L. Wamboldt, G. Seward, T. Haas, R. Chapman, Thin films of WO_3 for practical electrochromic windows. *Sol. Energy Mater.* **16**, 365–370 (1987).
48. V. Srinivas, J. Hryniewicz, Y. J. Chen, C. E. C. Wood, Intrinsic linewidths and radiative lifetimes of free excitons in GaAs quantum wells. *Phys. Rev. B* **46**, 10193–10196 (1992).
49. T. H. Gfroerer, Photoluminescence in analysis of surfaces and interfaces. *Encycl. Anal. Chem.* 10.1002/9780470027318.a2510 (2006).
50. J. Zultak, S. J. Magorrian, M. Koperski, A. Garner, M. J. Hamer, E. Tóvári, K. S. Novoselov, A. A. Zhukov, Y. Zou, N. R. Wilson, S. J. Haigh, A. V. Kretinin, V. I. Fal'ko, R. Gorbachev, Ultra-thin van der Waals crystals as semiconductor quantum wells. *Nat. Commun.* **11**, 125 (2020).
51. C. Hsu, R. Frisenda, R. Schmidt, A. Arora, S. M. de Vasconcellos, R. Bratschitsch, H. S. J. van der Zant, A. Castellanos-Gomez, Thickness-dependent refractive index of 1L, 2L, and 3L MoS_2, $MoSe_2$, WS_2, and WSe_2. *Adv. Opt. Mater.* **7**, 1900239 (2019).
52. D. E. Aspnes, A. A. Studna, Dielectric fuctions and optical parameters of Si, Ge, GaP, GaAs, GaSb, InP, InAs, and InSb from 1.5 to 6.0 eV. *Phys. Rev. B* **27**, 985–1009 (1983).
53. L. V. Rodríguez-de Marcos, J. I. Larruquert, J. A. Méndez, J. A. Aznárez, Self-consistent optical constants of SiO_2 and Ta_2O_5 films. *Opt. Mater. Express* **6**, 3622–3637 (2016).

Acknowledgments

Funding: This work was supported by the Samsung Research Funding Center of Samsung Electronics (Project Number: SRFC-MA1502-12) and the National Research Foundation (NRF) of Korea [2017R1A5A1014862 (SRC Program: vdWMRC Center) and 2020R1A2C2009389]. C.-H.L. acknowledges the support from the KU-KIST School Project. G.-H.L. acknowledges the support from the Korea Institute of Energy Technology Evaluation and Planning (KETEP) and the Ministry of Trade, Industry & Energy (MOTIE) (20173010013340) of the Republic of Korea. H.-G.P. acknowledges the support from the NRF of Korea (grant 2018R1A3A3000666). H.Y.J. acknowledges the support from the NRF of Korea (2018R1A2B6008104). **Author contributions:** C.-H.L. and G.-H.L. conceived the idea and supervised the project. Y.S.K., S.K., and D.L. performed the experiments and analyzed the data. S.K. performed the numerical simulation. J.-P.S., S.L., and H.-G.P. carried out low-temperature optical measurements. J.C.K. and H.Y.J. prepared and observed the cross-sectional STEM samples. K.K. and H.C. performed the Raman measurements. S.Y. performed the bandgap analyses. Y.J. and Y.S. provided large-area samples. Y.S.K., G.-H.L., and C.-H.L. wrote the manuscript. All authors discussed the results and commented on the manuscript. **Competing interests:** The authors declare that they have no competing interests. **Data and materials availability:** All data needed to evaluate the conclusions in the paper are present in the paper and/or the Supplementary Materials. Additional data related to this paper may be requested from the authors.

Submitted 13 July 2020
Accepted 10 February 2021
Published 26 March 2021
10.1126/sciadv.abd7921

Citation: Y. S. Kim, S. Kang, J.-P. So, J. C. Kim, K. Kim, S. Yang, Y. Jung, Y. Shin, S. Lee, D. Lee, J.-W. Park, H. Cheong, H. Y. Jeong, H.-G. Park, G.-H. Lee, C.-H. Lee, Atomic–layer–confined multiple quantum wells enabled by monolithic bandgap engineering of transition metal dichalcogenides. *Sci. Adv.* **7**, eabd7921 (2021).